

A sample of 1959 massive galaxy clusters at high redshifts

Z. L. Wen^{1,2*} and J. L. Han^{1,2,3 †}

1. National Astronomical Observatories, Chinese Academy of Sciences, 20A Datun Road, Chaoyang District, Beijing 100012, China

2. CAS Key Laboratory of FAST, NAOC, Chinese Academy of Sciences, Beijing 100101, China

3. School of Astronomy, University of Chinese Academy of Sciences, Beijing 100049, China

Accepted XXX. Received YYY; in original form ZZZ

ABSTRACT

We identify a sample of 1959 massive clusters of galaxies in the redshift range of $0.7 < z < 1.0$ from the survey data of Sloan Digital Sky Survey (SDSS) and Wide-field Infrared Survey Explorer (WISE). These clusters are recognized as the overdensity regions around the SDSS luminous red galaxies, having a richness greater than 15 or an equivalent mass $M_{500} \geq 2.5 \times 10^{14} M_{\odot}$. Among them, 1505 clusters are identified for the first time, which significantly enlarge the number of high-redshift clusters of $z > 0.75$. By comparing them with clusters at lower redshifts, we confirm that richer clusters host more luminous brightest cluster galaxies (BCGs) also at high redshifts, and that the fraction of blue galaxies is larger in clusters at higher redshifts. A small fraction of BCGs show ongoing star formation or active nuclei. The number density profile of member galaxies in stacked samples of clusters shows no significant redshift evolution.

Key words: catalogues — galaxies: clusters: general — galaxies: evolution

1 INTRODUCTION

The formation and evolution of clusters have become a hot subject in astrophysics for decades (see a review in Kravtsov & Borgani 2012). As the largest gravitationally bound system, clusters of galaxies are formed at knots of the cosmic web. Clusters at higher redshifts possess more star-forming galaxies with a blue color, which is known as the Butcher–Oemler effect (Butcher & Oemler 1978, 1984; Dressler et al. 1997). The member galaxies of clusters in the local universe are dominated by red early-type galaxies (Rood 1969; Binggeli et al. 1987; Ferguson & Sandage 1991). However, the progenitors of clusters known as protoclusters are usually dominated by star-forming galaxies at redshifts $z > 2$ (Miley et al. 2004; Venemans et al. 2007; Capak et al. 2011). The stellar population in most brightest cluster galaxies (BCGs) was also formed at redshifts $z > 2$ and evolved passively afterwards (Whiley et al. 2008; Stott et al. 2008; Wen & Han 2011), but stellar mass of BCGs increases significantly with time by accreting satellite galaxies (De Lucia & Blaizot 2007; Lidman et al. 2012; Bellstedt et al. 2016). Evolution studies of cluster properties require a large sample of clusters covering a wide redshift range.

Recent years, the Sloan Digital Sky Survey (SDSS, York et al. 2000) provides a great data base to identify large samples of galaxy clusters to a redshift of $z \sim 0.8$ (Koester et al. 2007; Wen et al. 2009; Hao et al. 2010; Szabo et al. 2011; Wen et al. 2012; Rykoff et al. 2014; Oguri 2014; Wen & Han 2015; Rykoff et al. 2016; Banerjee et al. 2018). Massive clusters up to redshifts of $z \sim$

1.6 have been identified and spectroscopically confirmed by optical and infrared observations (Stanford et al. 2005; Castellano et al. 2007; Kurk et al. 2009; Wilson et al. 2009; Papovich et al. 2010; Chiaberge et al. 2010; Stanford et al. 2012). Larger samples of high-redshift clusters have been identified from deep multi-band photometric surveys. Gladders & Yee (2005) identified 429 cluster candidates at redshifts $0.2 < z < 1.4$ from the 10.13 square degree area of Red-Sequence Cluster Survey. Goto et al. (2008) identified 16 galaxy clusters at redshifts $0.9 < z < 1.7$ from the 0.4 square degree AKARI data. Zatloukal et al. (2007) identified 12 cluster candidates at redshifts $1.23 \leq z \leq 1.55$ from the 0.66 square degree area of Cosmic Evolution Survey (COSMOS). van Breukelen et al. (2006) identified 13 clusters at redshifts $0.61 \leq z \leq 1.39$ from the 0.5 square degree area of UKIRT Infrared Deep Sky Survey Early Data Release. Eisenhardt et al. (2008) identified 335 galaxy cluster and group candidates using the 4.5 μm -selected sample of objects from the 7.25 square degree area of Spitzer Infrared Array Camera Shallow Survey. Wen & Han (2011) identified 631 clusters, 202 clusters, 187 clusters and 737 clusters in a redshift range of $0.1 < z < 1.6$ respectively from the 35 square degree area of Canada-France-Hawaii Telescope (CFHT) Wide survey, the 3.2 square degree area of CFHT Deep survey, the 2.0 square degree area of COSMOS, and the 33 square degree area of Spitzer Wide-area InfraRed Extragalactic survey. Oguri et al. (2018) identified 1921 clusters at redshifts $0.1 < z < 1.1$ from the 232 square degree area of Hyper Suprime-Cam (HSC) Subaru Strategic Program. Searching for these high-redshift clusters from optical and infrared deep surveys were made over a sky area of only a few hundred square degrees, and only a few hundred massive clusters with a mass $> 10^{14} M_{\odot}$

* E-mail: zhonglue@nao.cas.cn

† E-mail: hjl@nao.cas.cn

at redshifts $z > 0.75$ have been recognized. In addition, a few tens X-ray massive clusters at redshifts $z > 0.75$ were found from many small fields of deep X-ray surveys (Jones et al. 1998; Piffaretti et al. 2011; Fassbender et al. 2011; Šuhada et al. 2012; Clerc et al. 2014; Finoguenov et al. 2010; Pacaud et al. 2016), and another a few tens clusters of redshifts $z > 0.75$ were found via the Sunyaev-Zel'dovich (SZ) effect on the sky surveys of cosmic microwave background by Planck satellite, Atacama Cosmology Telescope (ACT), and South Pole Telescope (SPT) (Marriage et al. 2011; Hasselfield et al. 2013; Bleem et al. 2015; Planck Collaboration et al. 2016).

Wide-field Infrared Survey Explorer (WISE, Wright et al. 2010) is an all sky survey in four mid-infrared bands. The currently largest sample of 47,600 clusters with a redshift of $0.025 < z < 0.4$ have been identified from the combined data of Two Micron All Sky Survey, WISE, and SuperCOSMOS covering 28,000 square degrees of the sky (Wen et al. 2018). Because of the $1.6 \mu\text{m}$ bump in the spectral energy distributions, the magnitudes of early-type galaxies in the WISE bands vary with redshift significantly slower than optical magnitudes in the redshift range of $0.5 < z < 1.5$ (Yan et al. 2013). Hence, the WISE data have a good advantage to detect a large sample of galaxy clusters up to a redshift of $z \sim 1$. By using WISE and SDSS photometric data and follow-up spectroscopy, Gettings et al. (2012) made the Massive Distant Clusters of Wise Survey, and reported their first discovery of a massive high-redshift cluster at a redshift of $z = 0.99$. Another 20 massive clusters at redshifts of $0.7 < z < 1.2$ have been confirmed later (Stanford et al. 2014; Gonzalez et al. 2015).

In this paper, we present a large sample of 1959 massive clusters of galaxies of $0.7 < z < 1$ identified from the data of SDSS and WISE covering ~ 10000 square degrees of the sky, and 1505 of them are recognized for the first time. In Section 2, we first describe the galaxy data and the identification procedures for high-redshift galaxy clusters. In Section 3, we study the evolution of cluster properties, including color evolution of BCGs, the fraction of blue galaxies in clusters and the number density profile of cluster member galaxies. A short summary is presented in Section 4.

Throughout this paper, we assume a flat Lambda cold dark matter cosmology taking $H_0 = 70 \text{ km s}^{-1} \text{ Mpc}^{-1}$, $\Omega_m = 0.3$ and $\Omega_\Lambda = 0.7$.

2 CLUSTERS OF GALAXIES IDENTIFIED FROM THE SDSS AND WISE

The high-redshift massive clusters are identified from the WISE data and the SDSS data by following a few steps. The luminous red galaxies (LRGs) with spectroscopic redshifts in the SDSS are first taken as BCG candidates. The photometric data of the SDSS are used to discard stars and low-redshift galaxies in the WISE catalogue. Galaxy clusters are then recognized as the overdensity regions in the remaining WISE source catalogue around the LRGs.

2.1 Galaxy data

The SDSS¹ performs the optical photometric survey and the follow-up spectroscopic survey in the northern sky (York et al. 2000). The photometric data have been taken at five broad bands (u , g , r , i , and z) covering 14,000 square degrees of

the sky (Aihara et al. 2011) reaching a limit of $r = 22.2 \text{ mag}$ (Stoughton et al. 2002). Among 278 million sources from the photometric data, 112 million sources have been classified as stars, and other 166 million sources are classified as galaxies. All galaxies have their photometric redshifts estimated already (Brescia et al. 2014). The SDSS spectroscopic survey has been made to the galaxies with an extinction-corrected Petrosian magnitude of $r < 17.77$ for the main galaxy sample (Strauss et al. 2002) and the LRGs of $r < 19.5$ selected by using the gri magnitudes in the SDSS-I and II phases (Eisenstein et al. 2001). The SDSS-III Baryon Oscillation Spectroscopic Survey (BOSS) has completed the spectroscopic observations of the LRGs of $i < 19.9$ to a redshift of $z \sim 0.7$ covering ~ 10000 square degrees of the sky (Aihara et al. 2011). The SDSS-IV extended BOSS (eBOSS) further observed the LRGs in the redshift range of $0.6 < z < 1.0$ selected from the photometric data of the SDSS and WISE in the BOSS region covering 7500 square degrees of the sky (Prakash et al. 2016). In this work, we take the spectroscopic redshifts of galaxies from the latest SDSS Data Release 14 (DR14, Abolfathi et al. 2017), include the data of SDSS-III covering 10000 square degrees of the sky and the latest eBOSS data covering 2480 square degrees of the sky. According our previous result (Wen et al. 2012), most of BCGs are LRGs. We therefore take the 296,832 LRGs as BCG candidates, which all have spectroscopic redshifts observed ready. Contaminating active galactic nuclei are removed by setting the ‘spectra class = GALAXY’ and ‘zWaring = 0’.

The WISE survey² observes the whole sky in four mid-infrared bands (Wright et al. 2010): $W1$ ($3.4 \mu\text{m}$), $W2$ ($4.6 \mu\text{m}$), $W3$ ($12 \mu\text{m}$), and $W4$ ($22 \mu\text{m}$) with 5σ magnitude limits of 17.1, 15.7, 11.5, and 7.7 mag in the Vega system for point sources, respectively. In the SDSS BOSS region, we get 84 million WISE sources with a detection signal-to-noise greater than 10 in the $W1$ band, the fraction of saturation pixels of ‘wlsat < 5%’, and the contamination flag of ‘ccflag = 0000’. This magnitude limit in the $W1$ band corresponds to $0.7 L^*$ at $z = 0.7$ and slightly increases to $0.9 L^*$ at $z = 1$, here L^* is the characteristic luminosity of galaxies in clusters (Mancone et al. 2010). We convert the Vega magnitudes to AB magnitudes for the WISE sources by adding the offsets of 2.699, 3.339, 5.174, and 6.620 for $W1$, $W2$, $W3$ and $W4$ magnitudes, respectively (Jarrett et al. 2011).

For high-redshift galaxies, the $W1$ -band photometric data of WISE are deeper than the SDSS data due to the slow change of galaxy magnitude with redshift (Yan et al. 2013). We therefore identify high-redshift clusters from the WISE source catalogue, after foreground objects are discarded by using the SDSS photometric data. Considering the resolution of WISE data, we first remove the WISE sources within 3 arcsec of the known SDSS stars, and then remove the WISE sources within 3 arcsec of the known SDSS galaxies with a photometric redshift of $z < 0.65$ (otherwise $z < 0.7$ but considering the uncertainties photometric redshifts). After these foreground objects removed, we finally get only 27 million sources from the foreground-cleaned SDSS-WISE data, which are used for further identification of high-redshift massive clusters of $0.7 < z < 1$ (see Section 2.3).

2.2 The scaling relations for cluster radius and mass

The radius and mass are two fundamental parameters for galaxy clusters, and their scaling relations to observational data are the

¹ <http://www.sdss.org/>

² <http://irsa.ipac.caltech.edu/Missions/wise.html>

Table 1. The 1959 massive clusters of galaxies identified from the SDSS and WISE.

Name (1)	R.A. (2)	Dec. (3)	z (4)	i_{BCG} (5)	$W1_{\text{BCG}}$ (6)	SNR (7)	r_{500} (8)	L_{500} (9)	$R_{L*,500}$ (10)	M_{500} (11)	N_{sp} (12)	Other catalogues (13)
WH J000133.5−085212	0.38965	−8.86999	0.7938	19.51	17.25	8.12	0.75	13.61	15.73	2.59	10	
J000223.3−051523	0.59721	−5.25636	0.7044	19.52	17.55	5.78	0.73	15.36	15.47	2.54	10	WH15
WH J000309.8+082208	0.79096	8.36882	0.7370	19.61	18.02	6.42	0.76	17.36	18.40	3.06	12	
WH J000311.3+020653	0.79696	2.11459	0.8733	20.48	18.20	7.05	0.57	13.36	17.35	2.87	10	
WH J000354.1+304223	0.97556	30.70643	0.7398	19.86	17.62	6.46	0.86	18.50	19.69	3.29	18	
WH J000410.1+061513	1.04228	6.25357	0.8071	19.95	17.87	7.09	0.68	15.02	17.71	2.94	12	
WH J000419.7+335417	1.08207	33.90479	0.7258	19.47	17.70	7.26	0.76	17.18	17.90	2.97	14	
WH J000452.1+261003	1.21715	26.16741	0.8176	20.22	17.90	5.54	0.80	18.56	22.22	3.75	16	
WH J000546.7+022256	1.44453	2.38212	0.8397	20.52	17.45	7.98	0.77	13.84	17.12	2.83	9	
WH J000800.6+095535	2.00246	9.92629	0.7236	19.72	17.74	5.40	0.86	21.94	22.78	3.86	17	

Note. Column 1: Cluster name with J2000 coordinates of cluster and the suffix of “WH” indicating the new identification in this paper; Column 2 and 3: Right Ascension (R.A. J2000) and Declination (Dec. J2000) of cluster BCG (in degree); Column 4: spectroscopic redshift of the cluster; Column 5–6: BCG magnitudes in i and $W1$, respectively; Column 7: signal-to-noise ratio for cluster detection; Column 8: cluster radius, r_{500} , in Mpc; Column 9: L_{500} in units of L^* ; Column 10: cluster richness. Column 11: M_{500} in units of $10^{14} M_{\odot}$; Column 12: number of member galaxy candidates within r_{500} ; Column 13: other catalogue containing the cluster: RCS (Gladders & Yee 2005), SDSSCG (McConnachie et al. 2009), MCXC (Piffaretti et al. 2011), GMB+11 (Geach et al. 2011), WH11 (Wen & Han 2011), DAC+11 (Durret et al. 2011), WHL12 (Wen et al. 2012), XMMXCS (Mehrtens et al. 2012), SKT+12 (Shan et al. 2012), ACT (Hasselfield et al. 2013; Hilton et al. 2018), 2XMMi-SDSS (Takey et al. 2013, 2014), WH15 (Wen & Han 2015), BSG+15 (Buddendiek et al. 2015), DAB+15 (Durret et al. 2015), SWXCS (Liu et al. 2015) CAMIRA-HSC (Oguri et al. 2018).

(This table is available in its entirety in a machine-readable form.)

base for cluster identification. The cluster radius, r_{500} , is the radius within which the mean density of a cluster is 500 times of the critical density of the universe, and M_{500} is the cluster mass within r_{500} . Before identifying clusters, we first have to find out the scaling relations for estimating cluster radius and mass by using the cleaned SDSS-WISE data (without galaxies of $z < 0.65$).

As done in our previous papers (Wen et al. 2012; Wen & Han 2015), we get the scaling relations between the total $W1$ -band luminosities and known r_{500} (and M_{500}) of clusters compiled from literature. As listed in Table A, we compile the cluster masses M_{500} for 45 known clusters at redshifts $0.7 \leq z \lesssim 1$. These clusters are located in the SDSS region and have the SDSS-WISE data as discussed above. We recognize the member galaxy candidates in the cleaned SDSS-WISE data for each galaxy cluster, supposing that they are fainter than the BCG. The total $W1$ -band luminosity is calculated by summing the luminosities of all member galaxy candidates. Follow Wen et al. (2012) and Wen & Han (2015), the local background is estimated from an annulus of projected distance between 2–4 Mpc from the BCG candidate, and then subtracted from the total $W1$ -band luminosity. As shown in the appendix, we find that the radius r_{500} is related to total $W1$ -band luminosity within a radius of 1 Mpc from a BCG $L_{1\text{Mpc}}$ (in units of L^*) and redshift z by

$$\log r_{500} = 0.45 \log L_{1\text{Mpc}} - (0.81 \pm 0.12) + (0.57 \pm 0.29) \log(1+z). \quad (1)$$

We then calculate the total $W1$ -band luminosity L_{500} (also in units of L^*) within the radius of r_{500} , and then find that cluster mass M_{500} (in units of $10^{14} M_{\odot}$) is scaled with L_{500} and z by

$$\log M_{500} = 1.08 \log L_{500} - (1.50 \pm 0.29) + (2.69 \pm 0.70) \log(1+z). \quad (2)$$

The richness $R_{L*,500}$ is thus defined as a mass proxy by

$$R_{L*,500} = L_{500} \left(\frac{1+z}{1+0.7} \right)^{2.69}, \quad (3)$$

so that the cluster mass and the richness is related by

$$\log M_{500} = 1.08 \log R_{L*,500} - (0.88 \pm 0.20). \quad (4)$$

2.3 Identification of galaxy clusters

Clusters of galaxies always stand out clearly in optical/infrared data as overdensity regions of galaxies around luminous BCGs (Abell 1958; Abell et al. 1989). Following our previous papers (Wen et al. 2009; Wen & Han 2011, 2015; Wen et al. 2018), we identify massive high-redshift clusters from the cleaned SDSS-WISE data with the following steps:

1. Find an overdensity region around each BCG candidate. We take each observed LRG as a BCG candidate, which has a spectroscopic redshift determined already in the SDSS. We calculate the total $W1$ -band luminosity $L_{0.5}$ of member galaxy candidates within a projected radius of 0.5 Mpc around the BCG candidate, within which a rich cluster can have enough member galaxies (Girardi et al. 1995; Adami et al. 1998). We then have to estimate the local “background” and also the “fluctuation” of the total luminosity of galaxies. For each cluster candidate, $\langle L_{0.5} \rangle$ is estimated locally by the galaxies within an annulus of projected distance between 2–4 Mpc from the BCG candidate. To get the fluctuation $\sigma_{L_{0.5}}$, we randomly select 1000 positions on the sky, and obtain the deviation of 1000 total luminosities of $L_{0.5}$. An overdensity region with a high “signal-to-noise ratio”, $\text{SNR} = (L_{0.5} - \langle L_{0.5} \rangle) / \sigma_{L_{0.5}} \geq 5$, is identified as a cluster candidate. Obviously a larger SNR means a larger number of galaxies or more luminous galaxies in the area with a photometric redshift of $z > 0.65$.

2. Estimate the cluster radius and richness of the cluster candidate by using the scaling relations described above. We first calculate the total $W1$ -band luminosity, $L_{1\text{Mpc}}$, within a radius of 1 Mpc around the BCG from the cleaned SDSS-WISE data, so that r_{500} can be estimated by using the equation (1). Afterwards, the total luminosity L_{500} can be obtained from the cleaned SDSS-WISE

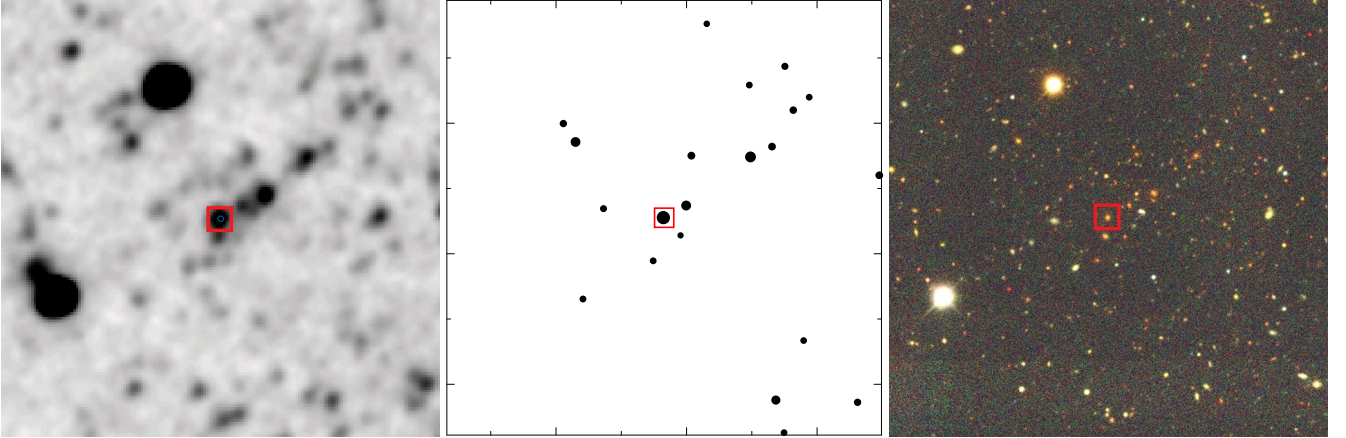


Figure 1. The $4' \times 4'$ images of a rich cluster at a redshift of $z = 0.8623$ identified from the foreground-cleaned SDSS-WISE data at R.A. = 4.76343° and Dec. = -0.01448° . The WISE $W1$ -band image in the left panel shows many galaxies concentrated around the BCG marked by the square. The black dots in the middle panel indicate the positions of member galaxy candidates, with a symbol size scaled by the square root of galaxy luminosities. The right panel shows the colour image of the cluster from the Dark Energy Survey (<https://des.ncsa.illinois.edu/releases/dr1/dr1-access>).

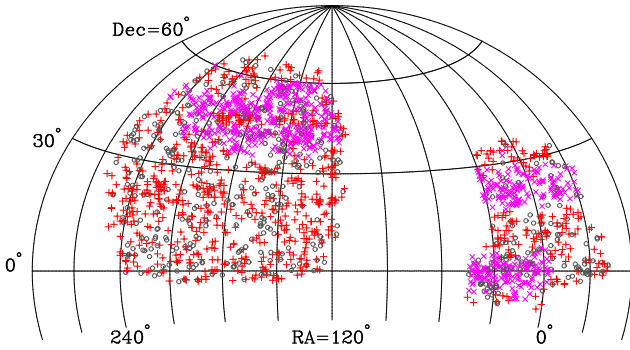


Figure 2. The sky distribution of 1959 clusters of galaxies identified in this paper: 454 previously known clusters are indicated by circles, and newly identified clusters are indicated by “+” or “x” if they are in the eBOSS region.

data, and the cluster richness $R_{L*,500}$ and finally the cluster mass M_{500} can be derived by using equation (3) and equation (4).

3. Clean the entries. It is possible that a rich cluster contains two or more LRGs with SDSS spectroscopic redshifts, which all are regarded as BCG candidates, so that a cluster can be sort out twice or more times in the above procedures. We therefore perform the friends-of-friends algorithm (Huchra & Geller 1982) to merge them into one cluster if they have a redshift difference smaller than 0.1 and a projected distance smaller than $1.5 r_{500}$. The BCG of the richest one is then adopted for such a multi-identified cluster.

Figure 1 show an example of a newly identified massive cluster, WH J001903.2–000052, at a redshift of $z = 0.8625$ with a richness of $R_{L*,500} = 34.35$ and a SNR = 9.10. Due to faint optical magnitudes of member galaxies, this cluster was not identified in previous papers based on the SDSS data. The WISE $W1$ -band image is deeper for high-redshift galaxies than the SDSS data, and shows many sources around the central BCG. After discarding the foreground objects, the distribution of member galaxy candidates shows a clear overdensity of galaxies around the BCG. The colour

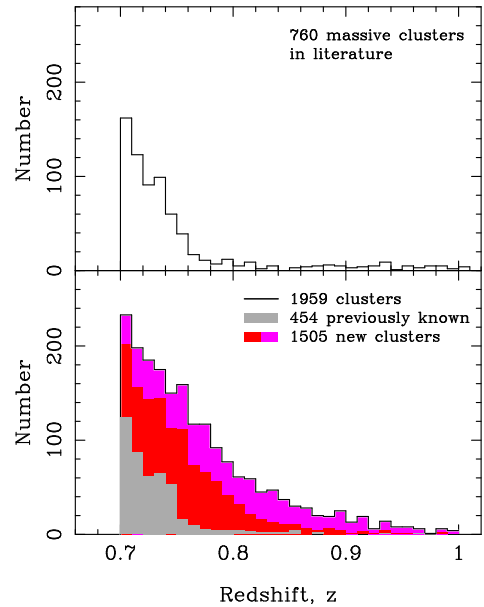


Figure 3. Redshift distribution of the 1959 massive high-redshift clusters (lower panel), compared with all known massive clusters from literature (upper panel). The newly identified 1505 clusters significantly enlarge the high-redshift cluster sample of $z > 0.75$, and clusters of $z > 0.8$ are mostly detected in the eBOSS region (cf. Figure 2).

image from Dark Energy Survey³ confirms that the cluster contains many member galaxies with a similarly red colour.

In Table 1 we publish 1959 massive clusters identified in the SDSS BOSS region covering ~ 10000 square degrees (see Figure 2). The BCGs of all clusters have the spectroscopic redshifts observed already, which are taken as the redshift of the clusters. The redshift distribution of the clusters is in the range of $0.7 < z < 1$ as shown in Figure 3. Comparing to the redshift distribution of all known clusters we collected from literature in this redshift range (including 454 known clusters re-identified in this paper, see be-

³ <https://des.ncsa.illinois.edu/releases/dr1/dr1-access>

low), our 1505 newly identified clusters of galaxies significantly enlarge the sample of high-redshift clusters especially at a redshift of $z > 0.75$. The identified clusters have a richness of $R_{L*,500} \geq 15$ that corresponds to a mass of $M_{500} \geq 2.5 \times 10^{14} M_{\odot}$ according to equation (4). Obviously, only relatively luminous cluster members detected in the WISE $W1$ -band are used for the cluster finding. On average there are about 17 member galaxy candidates within r_{500} for each clusters (see column 12 of Table 1).

2.4 Matching with previous cluster catalogs

In the sky region of SDSS coverage, some of high-redshift galaxy clusters have previously been identified from the SDSS photometric data (e.g. Geach et al. 2011; Wen et al. 2012) or deep survey data in some small regions (e.g. Gladders & Yee 2005; Wen & Han 2011; Durret et al. 2011). We cross-match our identified clusters of galaxies with those in previous cluster catalogues to find out how many clusters are newly identified.

The largest catalogue that we made a few years ago comprises 132,684 clusters of $0.05 < z < 0.8$ from the SDSS photometric data (WHL12, Wen et al. 2012). By including spectroscopic redshifts of the SDSS DR12, Wen & Han (2015) updated the WHL12 cluster catalogue and identified additional 25,419 new clusters mostly with higher redshifts, from which we get 1696 clusters with a redshift of $z \geq 0.7$. We cross-match these 1696 clusters with 1959 clusters of this paper within a projected separation of $1.5 r_{500}$ and a redshift difference of $c\Delta z/(1+z) = 2500 \text{ km s}^{-1}$ if spectroscopic redshifts are available, otherwise a redshift difference of 0.05. We get 404 matches. By adding non-overlapping clusters in other catalogues (Gladders & Yee 2005; McConnachie et al. 2009; Wen & Han 2011; Durret et al. 2011; Geach et al. 2011; Piffaretti et al. 2011; Mehrrens et al. 2012; Shan et al. 2012; Hasselfield et al. 2013; Takey et al. 2013, 2014; Buddendiek et al. 2015; Durret et al. 2015; Liu et al. 2015; Oguri et al. 2018; Hilton et al. 2018), we finally have 454 clusters previously known and the rest 1505 clusters are newly recognized for the first time in this paper.

As shown in Figure 3, the identified clusters have a median redshift of about 0.75. In the redshift range of $z > 0.75$, however, 94% of the clusters are newly identified. Comparing with the redshift distribution of all 760 previously known massive clusters of $M_{500} \geq 2.5 \times 10^{14} M_{\odot}$ compiled from literature (references listed above, plus clusters outside the SDSS regions in Bleem et al. 2015; Pacaud et al. 2016; Planck Collaboration et al. 2016; Rykoff et al. 2016), one can see that our cluster sample significantly enlarges the number of high-redshift clusters. Because more LRGs with higher redshifts have been observed in the eBOSS region, the identified clusters are about three times more in the sky number density (about 0.28 per square degree) than those in the other BOSS region. Most of clusters of $z > 0.8$ are found around the LRGs in the eBOSS region.

We here estimate the detection rate of clusters identified from the cleaned SDSS-WISE data. There are 216 clusters (Wen & Han 2015) with a richness greater than 50 in this sky region, and the spectroscopic redshifts of their BCGs are available. We find that 131 (61%) of 216 clusters are detected. The detection rate is higher for richer clusters, increasing to 71% (76 of 107) for clusters with a WH15 richness greater than 60. Therefore, it is good to find out more high-redshift clusters as listed Table 1, while we aware that some massive clusters are still missing because they show a lower SNR or richness in the cleaned SDSS-WISE data.

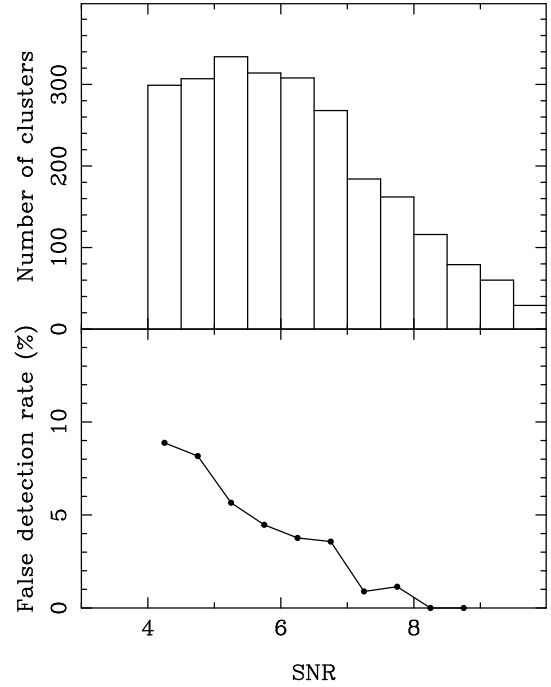


Figure 4. Distribution of cluster detection SNR (upper panel) and false detection rate as a function of SNR (lower panel).

2.5 The false detection rate

Galaxy clusters in Table 1 have been identified from the overdensity regions in the sky, and their member galaxies are possibly mixed with field galaxies. It is also possible that the projection effect from foreground or background filaments of the large scale cosmic web may lead to a false detection of galaxy clusters. Therefore, the false detection rate should be estimated for a cluster sample identified from optical/infrared photometric data.

We estimate the false detection rate by using a mock galaxy catalogue generated from the observed data (e.g., Goto et al. 2002; Koester et al. 2007; Hao et al. 2010; Wen et al. 2012). We start from the catalogue of WISE galaxies, in which low-redshift galaxies are kept temporally. We first remove the member galaxy candidates of clusters in this work and those of clusters in Wen & Han (2015) from the galaxy catalogue. Then, we generate a mock catalogue by randomly shuffling the magnitudes and photometric redshifts together for the rest galaxies, so that the positions of galaxies and the correlation between redshift and magnitude are all reserved. Subsequently we remove the low-redshift galaxies of $z < 0.65$. These procedures can eliminate real unidentified clusters, but the two dimensional distribution of galaxies are kept the same as the real sample. Afterwards, the BCG candidates with spectroscopic redshifts are randomly put on the sky, so that we can check if the projection effect leads to any false detections. We apply the same cluster identification procedures discussed above to the mock data, with the thresholds of $\text{SNR} \geq 4$ and $R_{L*,500} \geq 15$. Any detected “clusters” around the BCG candidates from the mock data therefore can be regarded as false detections. The false detection rate is calculated as being the ratio between the number of false detections from the mock data and the total number of identified clusters from the real data. Here, the false detection rate with $4 \leq \text{SNR} < 5$ is also calculated. To minimize the random noise, we generate ten such mock samples of galaxies and get an average false detection rate.

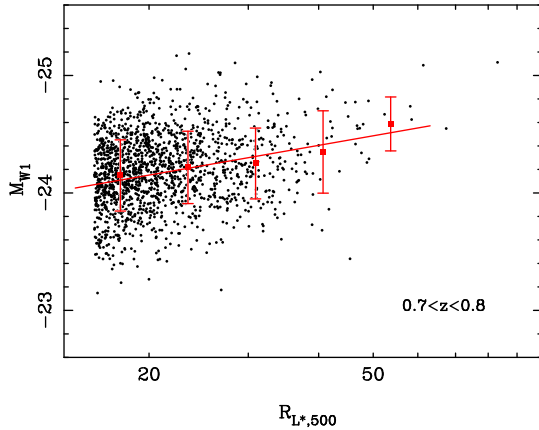


Figure 5. The correlation between the $W1$ -band absolute magnitude of BCGs and cluster richness confirms that richer clusters host more luminous BCGs.

As shown in Figure 4, the false detection rate depends on the signal-to-noise ratio SNR of the overdensity detection. It is negligible for $\text{SNR} > 8$, but increases with a smaller SNR. We therefore set the threshold of $\text{SNR} \geq 5$ so that the false detection rate is $\lesssim 5\%$ in each bin, and about 3% for the whole sample.

3 PROPERTIES OF CLUSTERS

Combining the clusters we identified at high redshifts in this paper with the massive clusters we previously identified at lower redshifts from the SDSS data, we can investigate the evolution of BCGs and cluster properties.

3.1 Evolution of BCGs

BCGs are the most massive galaxies located at the potential centres of clusters. Generally, they have an elliptical morphology but show different properties from normal elliptical galaxies (Schombert 1986; Bernardi et al. 2007; Liu et al. 2008). Optical and near-infrared data show that the color evolution of BCGs is in good agreement with a passive population synthesis model (Stott et al. 2008; Whiley et al. 2008; Wen & Han 2011). However, several studies show signatures of ongoing star formation or active galactic nuclei (AGN) in some BCGs (Crawford et al. 1999; McNamara et al. 2006; Liu et al. 2012; Fraser-McKelvie et al. 2014; Green et al. 2016; Donahue et al. 2017; Bonaventura et al. 2017).

Previously, we found that richer clusters host more luminous BCGs at redshifts $z < 0.42$ (Wen et al. 2012). Here we can investigate if it keeps true at a much higher redshift. For the clusters of $0.7 < z < 0.8$, the $W1$ -band absolute magnitudes of BCGs are obtained and then plotted against the cluster richness as shown in Figure 5. We find the best fit to the data as being

$$M_{W1} = (-23.02 \pm 0.24) - (0.87 \pm 0.16) \log R_{L*,500}, \quad (5)$$

which is very consistent with those for low-redshift clusters shown in figure 19 of Wen et al. (2012).

Wen & Han (2011) studied the optical colour evolution of BCGs by using a sample of clusters up to a redshift of $z \sim 1.6$. Here, we investigate the optical and mid-infrared colour evolution of BCGs in the redshift range of $0.05 < z < 1$ by using a combined sample of 9192 BCGs of massive clusters from this work and

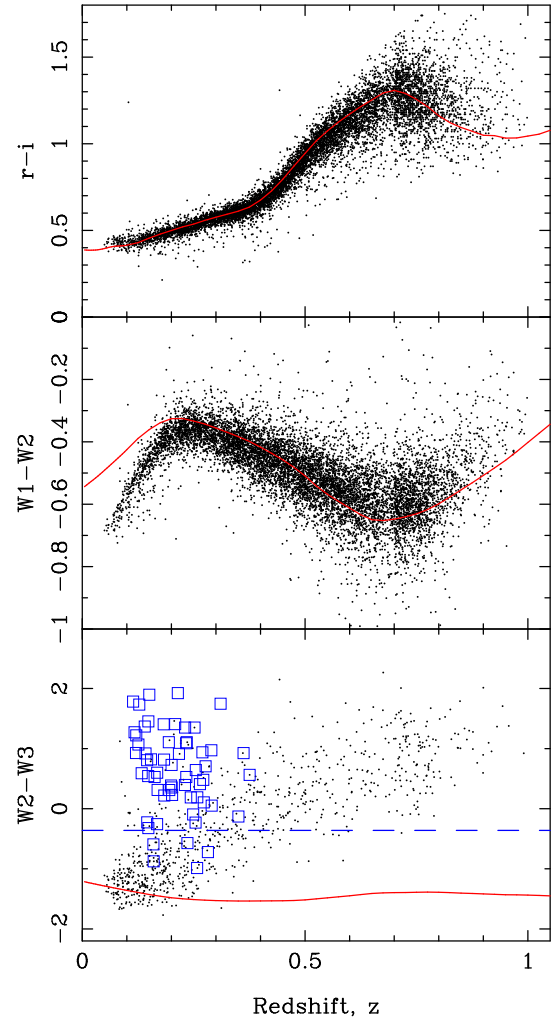


Figure 6. Evolution of colours of $r - i$ (top panel), $W1 - W2$ (middle panel) and $W2 - W3$ (bottom panel) as a function of redshift for 9192 BCGs in massive clusters. The solid lines represent the colour evolution calculated by using BC03 model in which stellar population was formed at $z_f = 3$ with passive stellar evolution tracks. In the bottom panel, only 835 BCGs are shown, and others are below the detection limit in $W3$ band. Above the dashed line are galaxies probably with ongoing star formation, which is verified by 59 BCGs from Liu et al. (2012) indicated by squares.

Wen & Han (2015, with a richness ≥ 50). We get the magnitude data of all these BCGs in the r , i , $W1$ and $W2$ bands, which should be dominated by old stellar populations. The magnitude data in the $W3$ band, however, is sensitive to star formation or nuclei activity (Yan et al. 2013; Jarrett et al. 2013), and they are available for only 835 of the 9192 BCGs with a detection threshold of signal-to-noise ratio greater than 3.

We first show the redshift evolution of the optical colour $r - i$ and mid-infrared colour $W1 - W2$ for the BCGs in Figure 6. To explain colour evolution, we calculate the colours by using a passive population synthesis model (Bruzual & Charlot 2003, hereafter BC03), in which stellar population was formed at a redshift of $z_f = 3$. We adopt the stellar evolution tracks of Padova 1994 (Girardi et al. 1996), the ‘Basel3.1’ stellar spectral library (Westera et al. 2002), and the initial mass function of Chabrier (2003) and the Solar metallicity in the model. We find that the colour data $r - i$ are in good agreement with the BC03 model.

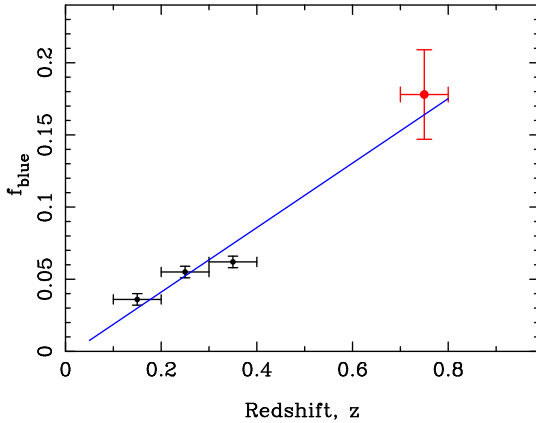


Figure 7. The fraction of blue member galaxies in clusters evolves as a function of redshift. The values at low redshift ($z < 0.4$, black dots) are obtained by using the SDSS data, and that at $z = 0.75$ by using the CFHT data. The solid line is the best fit to the data.

The distribution of mid-infrared colour $W1 - W2$ shows a peak at the redshift of $z \sim 0.2$ and a valley at the redshift of $z \sim 0.7$. The colour data $W1 - W2$ are marginally consistent with the BC03 model at redshifts $z > 0.2$, but are significantly lower than the model at redshifts $z \leq 0.2$. We noticed that the BC03 model was calibrated by using only the observed optical and near-infrared data (Bruzual & Charlot 2003). Obviously the mid-infrared WISE data here can provide good constraints on the population synthesis model of galaxies, which is beyond the scope of this paper.

In the bottom panel of Figure 6, we show the colour evolution of $W2 - W3$ for the 835 BCGs, which are marginally consistent with the BC03 model only at redshifts $z \leq 0.2$ but not at higher redshifts. For reference, we here take 59 BCGs from Liu et al. (2012), detected in the $W3$ band showing ongoing star formation with a star formation rate greater than $1 M_{\odot}/\text{yr}$. We find that 54 of the 59 BCGs have a colour of $W2 - W3 > -0.36$, which we adopt here as a criteria for deviating from the passive model (e.g. Green et al. 2016). Figure 6 shows that 428 of the 835 BCGs have a colour of $W2 - W3 > -0.36$. The rest BCGs without $W3$ detection may or may not have violent activities but can not be judged probably due to their high redshifts. We therefore conclude that at least 428 of 9192 ($\sim 4.6\%$) of BCGs in massive clusters have ongoing star formation or active nuclei.

3.2 Evolution of the fraction of blue galaxies

By using the clusters of $0.1 < z < 0.4$ from the SDSS (Wen & Han 2015) and the high-redshift clusters in this work, we verify the Butcher–Oemler effect, i.e. clusters at higher redshifts contain more blue member galaxies than those at lower redshifts (e.g. Butcher & Oemler 1978, 1984; Goto et al. 2003; Haines et al. 2009; Lerchster et al. 2011).

Considering that cluster galaxies of $M_r^e \leq -20.5$ are volume-limited complete to a redshift of $z \sim 0.4$ in the SDSS data, here M_r^e is the r -band evolution-corrected absolute magnitude defined in Wen et al. (2012), we take data of member galaxies of 2943 massive clusters with a richness ≥ 50 in the redshift range of $0.1 < z < 0.4$ (Wen & Han 2015). Those clusters have a comparable mass with the clusters we identified in this paper. We use the photometric redshifts to discriminate member galaxies of $M_r^e \leq -20.5$ (spectroscopic redshifts are used if available). The

photometric redshifts have been estimated for the SDSS galaxies to a limit of $r = 21.5$ with an uncertainty of $\sigma_z \simeq 0.023(1 + z)$ (Brescia et al. 2014). Member galaxies are obtained if they have a photometric redshift within a redshift slice of $1.6\sigma_z$ from a cluster redshift, so that about 90% member galaxies can be included within the redshift slice. Blue galaxies is defined to those with a rest-frame colour of $g - r$ bluer than the colour of cluster red sequence by 0.2 mag (Goto et al. 2003). We get the number of blue galaxies and the number of all galaxies in a cluster, after subtraction of the backgrounds estimated by using galaxies within the same redshift slice and the annulus of 2–4 Mpc from a cluster centre. We stack clusters in three redshift bins to get the averaged fractions of blue galaxies, as shown in Figure 7.

For the high-redshift clusters identified in this paper, we use the deeper CFHT Legacy Survey data⁴ to get their member galaxies. The latest T0007 data release⁵ covers about 155 square degrees in four independent fields (Hudelot et al. 2012), reaching a limit of $i \approx 23.5$ for extended sources (80% completeness) that is about 2 magnitude deeper than the SDSS data. The absolute magnitudes are available, and the galaxy photometric redshifts were estimated based on the methods of Ilbert et al. (2006) and Coupon et al. (2009) with a redshift uncertainty of $0.033(1 + z)$. The four CFHT fields are overlapped with the SDSS survey and we get member galaxies for 29 clusters of $0.7 < z < 0.8$ from the CFHT data. Following Goto et al. (2003), we find a fraction of blue galaxies $f_{\text{blue}} = 0.18 \pm 0.03$ at $z \sim 0.75$ (see Figure 7), much higher than those in clusters of $z < 0.4$, indicating that the blue fraction increases with redshift to $z \sim 0.8$. It is interesting to see $f_{\text{blue}} = (0.22 \pm 0.03)z \pm 0.01$ for those massive clusters with the blue galaxies criterion setting as bluer $g - r$ than the red sequence by 0.2 mag. However, we notice that in addition to the redshift evolution effect, the blue fraction depends on cluster mass, cluster-centric distance and galaxy magnitude (Postman et al. 2005; Hansen et al. 2009), which may explain the discrepancy between our result and the larger fractions obtained at similar redshifts in some previous works (e.g. Goto et al. 2003; De Lucia et al. 2007; Nishizawa et al. 2018).

3.3 Surface number density profile of member galaxies

The member galaxies of 2943 massive clusters with a richness ≥ 50 in the redshift range of $0.1 < z < 0.4$ and of 29 clusters of $0.7 < z < 0.8$ from the CFHT data can be used to investigate the evolution of surface number density profile of member galaxies. The three-dimensional number density profile of member galaxies can be described by the NFW model (Navarro et al. 1997)

$$\rho(r) = \frac{\rho_s}{\left(r/r_s\right)\left(1 + r/r_s\right)^2}, \quad (6)$$

where ρ_s and r_s are the characteristic density and radius, respectively. The concentration parameter for the NFW profile is defined as $c_{500} = r_{500}/r_s$. The projected surface density profile, Σ_{NFW} , is then obtained by integrating the profile along the light of sight (Bartelmann 1996).

We stack the clusters in four redshift bins and calculate the surface number density profiles of member galaxies out to the distance of $3r_{500}$, which are then fitted with the superposition of a

⁴ <http://www.cfht.hawaii.edu/Science/CFHLS/>

⁵ <http://terapix.iap.fr/>

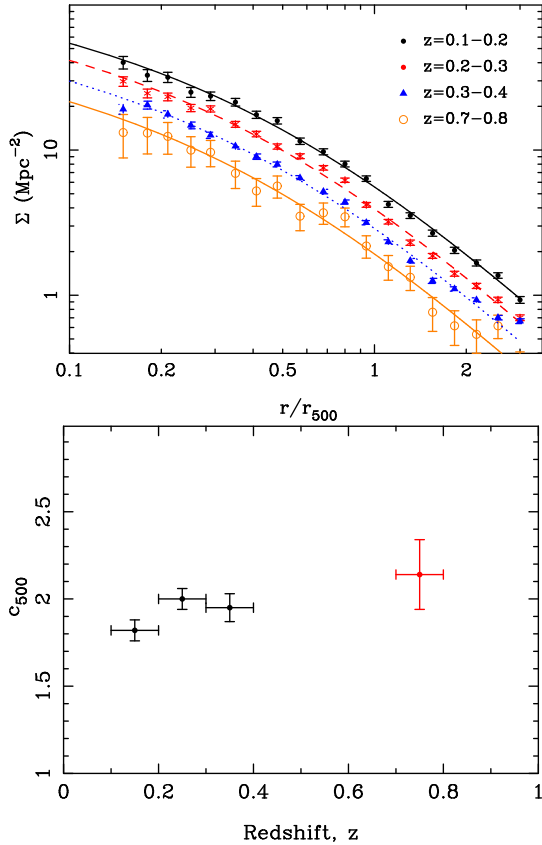


Figure 8. Surface number density profiles of member galaxies in different redshift bins are fitted with a projected NFW profile (upper panel). To show clearly, data points and fittings are shifted in the vertical direction by multiplying a factor of $10^{-0.1}$, $10^{-0.2}$ and $10^{-0.3}$ for $z = 0.2-0.3$, $z = 0.3-0.4$ and $z = 0.7-0.8$, respectively. The concentration parameter is plotted against redshift in the lower panel, showing no significant evolution.

projected NFW profile and a constant background

$$\Sigma(r/r_{500}) = \Sigma_{\text{NFW}} + \Sigma_{\text{back}}, \quad (7)$$

as shown in Figure 8. We find that the number density profile has no significant redshift evolution, consistent with the recent conclusions based on the SPT-SZ clusters of $z < 1.1$ (Zenteno et al. 2016; Hennig et al. 2017) and the clusters of $z < 1$ in the Subaru HSC Survey (Lin et al. 2017; Nishizawa et al. 2018). The concentration parameter of $c_{500} \sim 2$ is in agreement with those found by Hennig et al. (2017) and Lin et al. (2017).

4 SUMMARY

We identify a sample of 1959 massive galaxy clusters in the redshift range of $0.7 < z < 1.0$ by using the data from the SDSS and WISE, among which 1505 clusters are recognized for the first time. These clusters are identified around SDSS LRGs as being the overdensity regions of galaxies with a signal-to-noise ratio greater than 5. This cluster sample significantly enlarges the number of massive clusters at $z > 0.75$. We combine these high-redshift clusters with the clusters in a lower redshift range to study the evolution of BCGs and clusters. The data verify the Butcher-Omler effect, and show that richer clusters have more luminous BCGs even at a high redshift. A small fraction of BCGs show activities of star formation or

active nuclei. The profile of number density of member galaxies in these massive clusters does not evolve with redshift.

ACKNOWLEDGEMENTS

We thank the referee for valuable comments that helped to improve the paper. The authors are partially supported by the National Natural Science Foundation of China (Grant No. 11473034, U1731127), the Key Research Program of the Chinese Academy of Sciences (Grant No. QYZDJ-SSW-SLH021) and the strategic Priority Research Program of Chinese Academy of Sciences (Grant No. XDB23010200), and the Open Project Program of the Key Laboratory of FAST, NAOC, Chinese Academy of Sciences. Funding for the Sloan Digital Sky Survey IV has been provided by the Alfred P. Sloan Foundation, the U.S. Department of Energy Office of Science, and the Participating Institutions. SDSS acknowledges support and resources from the Center for High-Performance Computing at the University of Utah. The SDSS web site is www.sdss.org. This publication makes use of data products from the Wide-field Infrared Survey Explorer, which is a joint project of the University of California, Los Angeles, and the Jet Propulsion Laboratory/California Institute of Technology, funded by the National Aeronautics and Space Administration. This work is based in part on data products produced at Terapix available at the Canadian Astronomy Data Centre as part of the Canada-France-Hawaii Telescope Legacy Survey, a collaborative project of NRC and CNRS, and also based on observations obtained with MegaPrime/MegaCam, a joint project of CFHT and CEA/IRFU, at the Canada-France-Hawaii Telescope (CFHT) which is operated by the National Research Council (NRC) of Canada, the Institut National des Science de l'Univers of the Centre National de la Recherche Scientifique (CNRS) of France, and the University of Hawaii.

REFERENCES

- Abell G. O., 1958, *ApJS*, **3**, 211
- Abell G. O., Corwin Jr. H. G., Olowin R. P., 1989, *ApJS*, **70**, 1
- Abolfathi B., et al., 2017, preprint, ([arXiv:1707.09322](https://arxiv.org/abs/1707.09322))
- Adami C., Mazure A., Katgert P., Biviano A., 1998, *A&A*, **336**, 63
- Aihara H., et al., 2011, *ApJS*, **193**, 29
- Banerjee P., Szabo T., Pierpaoli E., Franco G., Ortiz M., Oramas A., Tornello B., 2018, *New Astron.*, **58**, 61
- Bartelmann M., 1996, *A&A*, **313**, 697
- Bellstedt S., et al., 2016, *MNRAS*, **460**, 2862
- Bernardi M., Hyde J. B., Sheth R. K., Miller C. J., Nichol R. C., 2007, *AJ*, **133**, 1741
- Binggeli B., Tammann G. A., Sandage A., 1987, *AJ*, **94**, 251
- Bleem L. E., et al., 2015, *ApJS*, **216**, 27
- Bonaventura N. R., et al., 2017, *MNRAS*, **469**, 1259
- Brescia M., Cavuoti S., Longo G., De Stefano V., 2014, *A&A*, **568**, A126
- Brodwin M., et al., 2015, *ApJ*, **806**, 26
- Bruzual G., Charlot S., 2003, *MNRAS*, **344**, 1000
- Buddendiek A., et al., 2015, *MNRAS*, **450**, 4248
- Butcher H., Oemler Jr. A., 1978, *ApJ*, **219**, 18
- Butcher H., Oemler Jr. A., 1984, *ApJ*, **285**, 426
- Capak P. L., et al., 2011, *Nature*, **470**, 233
- Castellano M., et al., 2007, *ApJ*, **671**, 1497
- Chabrier G., 2003, *PASP*, **115**, 763
- Chiaberge M., Capetti A., Macchetto F. D., Rosati P., Tozzi P., Tremblay G. R., 2010, *ApJ*, **710**, L107
- Clerc N., et al., 2014, *MNRAS*, **444**, 2723
- Coupon J., et al., 2009, *A&A*, **500**, 981

- Crawford C. S., Allen S. W., Ebeling H., Edge A. C., Fabian A. C., 1999, *MNRAS*, **306**, 857
- De Lucia G., Blaizot J., 2007, *MNRAS*, **375**, 2
- De Lucia G., et al., 2007, *MNRAS*, **374**, 809
- Donahue M., Connor T., Voit G. M., Postman M., 2017, *ApJ*, **835**, 216
- Dressler A., et al., 1997, *ApJ*, **490**, 577
- Durret F., et al., 2011, *A&A*, **535**, A65
- Durret F., et al., 2015, *A&A*, **578**, A79
- Eisenhardt P. R. M., et al., 2008, *ApJ*, **684**, 905
- Eisenstein D. J., et al., 2001, *AJ*, **122**, 2267
- Fassbender R., et al., 2011, *New Journal of Physics*, **13**, 125014
- Ferguson H. C., Sandage A., 1991, *AJ*, **101**, 765
- Finoguenov A., et al., 2010, *MNRAS*, **403**, 2063
- Fraser-McKelvie A., Brown M. J. I., Pimbblet K. A., 2014, *MNRAS*, **444**, L63
- Geach J. E., Murphy D. N. A., Bower R. G., 2011, *MNRAS*, **413**, 3059
- Gettings D. P., et al., 2012, *ApJ*, **759**, L23
- Girardi M., Biviano A., Giuricin G., Mardirossian F., Mezzetti M., 1995, *ApJ*, **438**, 527
- Girardi L., Bressan A., Chiosi C., Bertelli G., Nasi E., 1996, *A&AS*, **117**, 113
- Gladders M. D., Yee H. K. C., 2005, *ApJS*, **157**, 1
- Gonzalez A. H., et al., 2015, *ApJ*, **812**, L40
- Goto T., et al., 2002, *AJ*, **123**, 1807
- Goto T., et al., 2003, *PASJ*, **55**, 739
- Goto T., et al., 2008, *PASJ*, **60**, S531
- Green T. S., et al., 2016, *MNRAS*, **461**, 560
- Guennou L., et al., 2014, *A&A*, **561**, A112
- Haines C. P., et al., 2009, *ApJ*, **704**, 126
- Hansen S. M., Sheldon E. S., Wechsler R. H., Koester B. P., 2009, *ApJ*, **699**, 1333
- Hao J., et al., 2010, *ApJS*, **191**, 254
- Hasselfield M., et al., 2013, *J. Cosmology Astropart. Phys.*, **7**, 008
- Hennig C., et al., 2017, *MNRAS*, **467**, 4015
- Hicks A. K., et al., 2008, *ApJ*, **680**, 1022
- Hilton M., et al., 2018, *ApJS*, **235**, 20
- Huchra J. P., Geller M. J., 1982, *ApJ*, **257**, 423
- Hudelot P., et al., 2012, *VizieR Online Data Catalog*, **2317**
- Ilbert O., et al., 2006, *A&A*, **457**, 841
- Jarrett T. H., et al., 2011, *ApJ*, **735**, 112
- Jarrett T. H., et al., 2013, *AJ*, **145**, 6
- Jones L. R., Scharf C., Ebeling H., Perlman E., Wegner G., Malkan M., Horner D., 1998, *ApJ*, **495**, 100
- Koester B. P., et al., 2007, *ApJ*, **660**, 239
- Kravtsov A. V., Borgani S., 2012, *ARA&A*, **50**, 353
- Kurk J., et al., 2009, *A&A*, **504**, 331
- Lamer G., Hoefl M., Kohnert J., Schwoppe A., Storm J., 2008, *A&A*, **487**, L33
- Lerchster M., et al., 2011, *MNRAS*, **411**, 2667
- Lidman C., et al., 2012, *MNRAS*, **427**, 550
- Lin Y.-T., et al., 2017, *ApJ*, **851**, 139
- Liu F. S., Xia X. Y., Mao S., Wu H., Deng Z. G., 2008, *MNRAS*, **385**, 23
- Liu F. S., Mao S., Meng X. M., 2012, *MNRAS*, **423**, 422
- Liu T., et al., 2015, *ApJS*, **216**, 28
- Mancone C. L., Gonzalez A. H., Brodwin M., Stanford S. A., Eisenhardt P. R. M., Stern D., Jones C., 2010, *ApJ*, **720**, 284
- Mantz A., Allen S. W., Ebeling H., Rapetti D., Drlica-Wagner A., 2010, *MNRAS*, **406**, 1773
- Marriage T. A., et al., 2011, *ApJ*, **737**, 61
- McConnachie A. W., Patton D. R., Ellison S. L., Simard L., 2009, *MNRAS*, **395**, 255
- McNamara B. R., et al., 2006, *ApJ*, **648**, 164
- Mehrtens N., et al., 2012, *MNRAS*, **423**, 1024
- Miley G. K., et al., 2004, *Nature*, **427**, 47
- Navarro J. F., Frenk C. S., White S. D. M., 1997, *ApJ*, **490**, 493
- Nishizawa A. J., et al., 2018, *PASJ*, **70**, S24
- Oguri M., 2014, *MNRAS*, **444**, 147
- Oguri M., et al., 2018, *PASJ*, **70**, S20
- Pacaud F., et al., 2016, *A&A*, **592**, A2
- Papovich C., et al., 2010, *ApJ*, **716**, 1503
- Piffaretti R., Arnaud M., Pratt G. W., Pointecouteau E., Melin J.-B., 2011, *A&A*, **534**, A109
- Planck Collaboration et al., 2015, *A&A*, **581**, A14
- Planck Collaboration et al., 2016, *A&A*, **594**, A27
- Postman M., et al., 2005, *ApJ*, **623**, 721
- Prakash A., et al., 2016, *ApJS*, **224**, 34
- Reichert A., Böhringer H., Fassbender R., Mühlegger M., 2011, *A&A*, **535**, A4
- Rood H. J., 1969, *ApJ*, **158**, 657
- Rykoff E. S., et al., 2014, *ApJ*, **785**, 104
- Rykoff E. S., et al., 2016, *ApJS*, **224**, 1
- Schombert J. M., 1986, *ApJS*, **60**, 603
- Shan H., et al., 2012, *ApJ*, **748**, 56
- Stanford S. A., et al., 2005, *ApJ*, **634**, L129
- Stanford S. A., et al., 2012, *ApJ*, **753**, 164
- Stanford S. A., Gonzalez A. H., Brodwin M., Gettings D. P., Eisenhardt P. R. M., Stern D., Wylezalek D., 2014, *ApJS*, **213**, 25
- Stott J. P., Edge A. C., Smith G. P., Swinbank A. M., Ebeling H., 2008, *MNRAS*, **384**, 1502
- Stoughton C., et al., 2002, *AJ*, **123**, 485
- Strauss M. A., et al., 2002, *AJ*, **124**, 1810
- Szabo T., Pierpaoli E., Dong F., Pipino A., Gunn J., 2011, *ApJ*, **736**, 21
- Takey A., Schwoppe A., Lamer G., 2013, *A&A*, **558**, A75
- Takey A., Schwoppe A., Lamer G., 2014, *A&A*, **564**, A54
- Takey A., Durret F., Mahmoud E., Ali G. B., 2016, *A&A*, **594**, A32
- Venemans B. P., et al., 2007, *A&A*, **461**, 823
- Vikhlinin A., et al., 2009, *ApJ*, **692**, 1033
- Wen Z. L., Han J. L., 2011, *ApJ*, **734**, 68
- Wen Z. L., Han J. L., 2015, *ApJ*, **807**, 178
- Wen Z. L., Han J. L., Liu F. S., 2009, *ApJS*, **183**, 197
- Wen Z. L., Han J. L., Liu F. S., 2012, *ApJS*, **199**, 34
- Wen Z. L., Han J. L., Yang F., 2018, *MNRAS*, **475**, 343
- Westera P., Lejeune T., Buser R., Cuisinier F., Bruzual G., 2002, *A&A*, **381**, 524
- Whiley I. M., et al., 2008, *MNRAS*, **387**, 1253
- Wilson G., et al., 2009, *ApJ*, **698**, 1943
- Wright E. L., et al., 2010, *AJ*, **140**, 1868
- Yan L., et al., 2013, *AJ*, **145**, 55
- York D. G., et al., 2000, *AJ*, **120**, 1579
- Zatloukal M., Röser H.-J., Wolf C., Hippelein H., Falter S., 2007, *A&A*, **474**, L5
- Zenteno A., et al., 2016, *MNRAS*, **462**, 830
- Šuhada R., et al., 2012, *A&A*, **537**, A39
- van Breukelen C., et al., 2006, *MNRAS*, **373**, L26

APPENDIX A: SCALING RELATIONS OBTAINED FROM 45 KNOWN CLUSTERS

To get the scaling relations for cluster radius and mass from observational data, we compile the cluster masses M_{500} derived by X-ray or SZ measurements for 45 known clusters from literature (Lamer et al. 2008; Hicks et al. 2008; Vikhlinin et al. 2009; Mantz et al. 2010; Reichert et al. 2011; Piffaretti et al. 2011; Hasselfield et al. 2013; Takey et al. 2013, 2014; Guennou et al. 2014; Planck Collaboration et al. 2015; Gonzalez et al. 2015; Brodwin et al. 2015; Buddendiek et al. 2015; Planck Collaboration et al. 2016; Takey et al. 2016), which are located in the SDSS region within a redshift range of $0.7 \leq z \lesssim 1$. The average mass is taken if a cluster has two or more mass estimates available in literature.

The location of a BCG is taken as the cluster centre, and its redshift as the redshift of a cluster. For each galaxy cluster, we

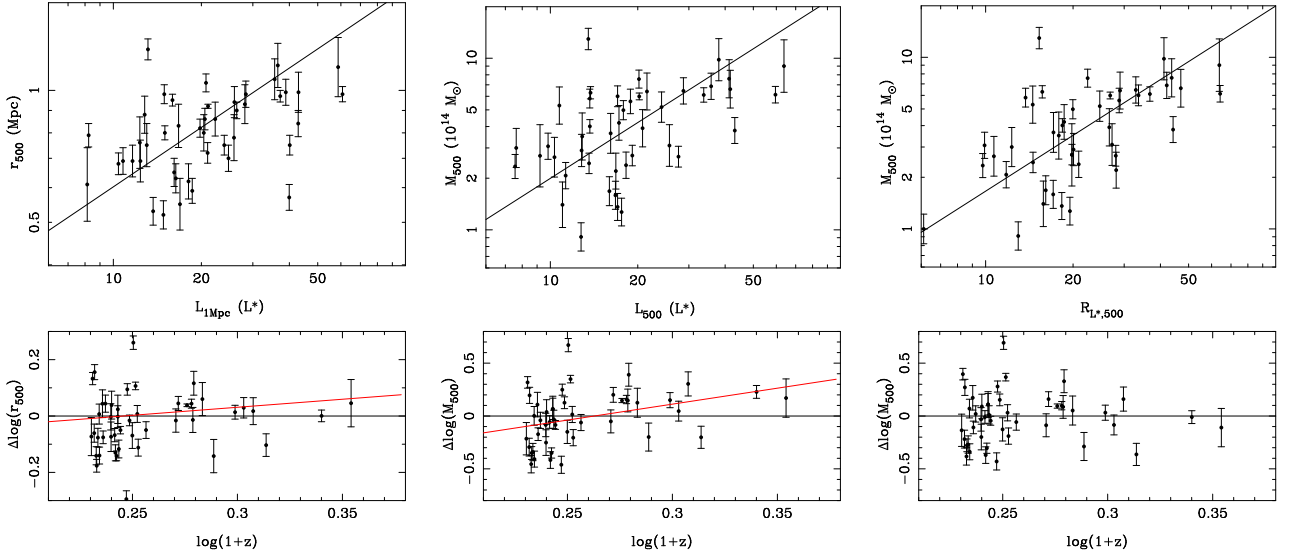


Figure A1. Upper panels show the scaling relations between cluster parameters derived from the WISE data (the X-axis) and cluster radius or mass (the Y-axis) for the 45 compiled clusters. The data deviations from the scaling relation are plotted in the lower panels to check the redshift dependence.

recognize the member galaxy candidates from the cleaned SDSS-WISE data to calculate a total *W*1-band luminosity. Galaxies with a spectroscopic redshift within a redshift slice of $c\Delta z/(1+z) = 2500 \text{ km s}^{-1}$ from the cluster redshift, z , are considered as member galaxies directly. Here c is the speed of light. Other galaxies in the cleaned WISE catalogue have no redshifts, and are adopted as cluster member galaxy candidates only if they are fainter than the BCG, because all stars and galaxies with a lower photometric redshift have been cleaned already. The total *W*1-band luminosity is then easily calculated by summing the luminosities of all member galaxy candidates. Follow the method in our previous papers (Wen et al. 2012; Wen & Han 2015), the local background is estimated from an annulus of projected distance between 2–4 Mpc from the BCG candidate, and then subtracted from the total *W*1-band luminosity.

We calculate the total *W*1-band luminosity within a radius of 1 Mpc from the BCG, $L_{1\text{Mpc}}$, in units of L^* which is the evolved characteristic luminosity of galaxies in the *W*1 band (Mancone et al. 2010). The left panel of Figure A1 shows the correlation between cluster radius r_{500} and $L_{1\text{Mpc}}$ for the 45 compiled clusters. Adopting a slope of 0.45 that was obtained by Wen & Han (2015), we find that the best fit to the data is

$$\log r_{500} = 0.45 \log L_{1\text{Mpc}} - (0.67 \pm 0.10), \quad (\text{A1})$$

where r_{500} is in units of Mpc and $L_{1\text{Mpc}}$ is in units of L^* . Noted that we use the flux-limited sample of WISE galaxies to calculate the total luminosity. Clusters at lower redshifts should contain more member galaxies than those at higher redshifts. The total luminosities of member galaxy candidates are then biased to smaller values at higher redshifts, so that the above relation may have a redshift dependence to check. We get the deviations of r_{500} from the above fitted relation, $\Delta \log r_{500} = \log r_{500} - (0.45 \log L_{1\text{Mpc}} - 0.67)$, and plot them against redshift. We find a slight dependence on redshift in the form of

$$\Delta \log r_{500} = (0.57 \pm 0.29) \log(1+z) - (0.14 \pm 0.07). \quad (\text{A2})$$

Considering this correction, the radius r_{500} is related to $L_{1\text{Mpc}}$ and

z by

$$\begin{aligned} \log r_{500} = & 0.45 \log L_{1\text{Mpc}} - (0.81 \pm 0.12) \\ & + (0.57 \pm 0.29) \log(1+z). \end{aligned} \quad (\text{A3})$$

Similar, we calculate the total *W*1-band luminosity L_{500} (also in units of L^*) within r_{500} for the 45 compiled clusters, certainly with a background subtraction. The cluster mass M_{500} and L_{500} are found to be closely correlated, as shown in the middle panel of Figure A1. Adopting a slope of 1.08 that was obtained by Wen & Han (2015), we find that the best fit to the data is

$$\log M_{500} = 1.08 \log L_{500} - (0.78 \pm 0.23), \quad (\text{A4})$$

where M_{500} is in units of $10^{14} M_{\odot}$. Again, to correct the redshift dependence, we get the deviations of M_{500} from the above fitted relation, $\Delta \log M_{500} = \log M_{500} - (1.08 \log L_{500} - 0.78)$, and plot them against redshift. We find a significant dependence on redshift in the form of

$$\Delta \log M_{500} = (2.69 \pm 0.70) \log(1+z) - (0.72 \pm 0.17). \quad (\text{A5})$$

Combining the last two equations, we get

$$\log M_{500} = 1.08 \log L_{500} - (1.50 \pm 0.29) \quad (\text{A6})$$

$$+ (2.69 \pm 0.70) \log(1+z). \quad (\text{A7})$$

We define the cluster richness by using the total *W*1-band luminosity L_{500} as being

$$R_{L^*,500} = L_{500} \left(\frac{1+z}{1+0.7} \right)^{2.69}. \quad (\text{A8})$$

The scaling relation between the cluster mass and the richness is given by

$$\log M_{500} = 1.08 \log R_{L^*,500} - (0.88 \pm 0.20), \quad (\text{A9})$$

which seems have no redshift bias as shown in the right panels of Figure A1.

Table A1. Parameters of 45 clusters with known mass (M_{500}) from literature

No. (1)	RA (2)	Dec. (3)	z (4)	M_{500} (5)	r_{500} (6)	Ref. (7)	$L_{1\text{Mpc}}$ (8)	L_{500} (9)
1	3.05893	16.03893	0.9440	1.40 ± 0.50	0.55 ± 0.08	B15a	16.90	11.01
2	5.55431	-0.60944	0.8050	6.86 ± 1.32	0.99 ± 0.07	H13	38.89	35.78
3	14.78542	-0.83494	0.7877	6.45 ± 1.24	0.98 ± 0.07	H13	28.39	28.73
4	19.99224	0.92608	0.7381	3.65 ± 1.12	0.83 ± 0.10	H13	16.71	16.13
5	31.55611	-1.23810	0.7146	5.19 ± 1.17	0.94 ± 0.08	H13	25.94	24.15
6	33.86876	0.51044	0.8650	3.91 ± 1.11	0.80 ± 0.08	H13	20.38	20.78
7	36.14264	-0.04238	0.7725	4.98 ± 0.68	0.90 ± 0.04	H08	26.42	17.84
8	37.12687	0.50991	0.7208	2.65 ± 0.81	0.75 ± 0.09	H13,T16	13.01	10.33
9	127.61035	52.69312	0.9900	5.60 ± 1.00	0.86 ± 0.05	L08	20.56	18.87
10	132.24341	44.86574	1.2600	2.70 ± 1.40	0.61 ± 0.13	R11	8.14	9.21
11	137.86015	5.83725	0.7682	7.56 ± 0.97	1.04 ± 0.05	P15	20.74	20.19
12	147.04832	29.11922	0.7780	6.60 ± 1.90	0.99 ± 0.11	B15b	42.96	41.66
13	155.64725	13.18128	0.7053	1.68 ± 0.36	0.65 ± 0.05	T14	16.14	15.97
14	156.95279	0.06054	0.7060	3.07 ± 0.59	0.79 ± 0.05	T14	8.23	9.82
15	162.01755	31.64720	0.7500	9.80 ± 3.20	1.14 ± 0.14	B15b	36.52	38.04
16	163.15559	57.51781	0.7090	0.91 ± 0.19	0.52 ± 0.04	T14	14.83	12.76
17	175.09245	66.13752	0.7843	6.29 ± 0.54	0.95 ± 0.03	P11,G14	15.93	13.75
18	175.69792	15.45319	1.1880	6.00 ± 0.90	0.82 ± 0.04	G15	19.79	17.04
19	178.94098	39.02004	1.0090	2.90 ± 0.70	0.69 ± 0.06	B15a	11.63	12.81
20	182.49605	49.89782	0.9020	5.30 ± 1.50	0.88 ± 0.09	B15b	12.80	10.74
21	186.68127	33.76685	0.7665	1.27 ± 0.26	0.57 ± 0.04	T14	39.95	17.59
22	186.74268	33.54683	0.8880	5.99 ± 0.28	0.92 ± 0.01	V09,M10	21.07	20.24
23	187.69325	10.94824	0.7519	1.00 ± 0.22	0.53 ± 0.04	T14	13.68	5.64
24	187.71085	41.57208	0.7454	1.36 ± 0.27	0.59 ± 0.04	T14	18.61	17.04
25	190.80023	13.21965	0.7896	2.38 ± 0.46	0.70 ± 0.05	T14	24.76	18.22
26	198.41559	22.19755	0.7370	3.10 ± 1.00	0.78 ± 0.10	B15b	25.86	25.71
27	201.20351	30.19414	0.7550	6.11 ± 0.62	0.97 ± 0.03	G14	37.21	33.75
28	204.38356	19.97465	0.9000	6.40 ± 1.80	0.93 ± 0.10	B15b	28.17	21.52
29	204.71948	4.72021	0.7264	2.07 ± 0.40	0.69 ± 0.05	T14	10.79	11.29
30	205.70715	40.47372	0.7099	2.67 ± 0.40	0.75 ± 0.04	P11	40.11	27.62
31	205.76897	-0.01547	0.7151	3.79 ± 0.72	0.84 ± 0.06	T14	42.87	43.17
32	208.43817	43.48428	0.7365	7.59 ± 2.21	1.06 ± 0.12	B15b,P16	35.62	41.28
33	213.79633	36.20111	1.0300	3.00 ± 0.90	0.69 ± 0.08	R11	12.37	7.63
34	217.27792	42.68572	0.9200	3.50 ± 1.30	0.76 ± 0.11	R11	12.32	12.87
35	217.80191	-0.10467	0.7122	1.59 ± 0.33	0.63 ± 0.05	T14	16.35	16.76
36	224.76913	52.81554	0.7023	5.82 ± 0.78	0.98 ± 0.05	P16	14.93	13.67
37	228.67696	13.78289	1.0590	2.20 ± 0.60	0.62 ± 0.06	B15a	18.07	16.81
38	229.48769	31.45816	0.7440	2.44 ± 0.36	0.72 ± 0.04	P11	21.01	13.59
39	231.63821	54.15210	0.7476	6.13 ± 0.72	0.98 ± 0.04	P16	60.76	59.59
40	231.92551	20.74407	0.7000	9.00 ± 3.80	1.13 ± 0.19	B15b	58.73	63.78
41	234.39471	38.48075	0.7500	4.20 ± 1.10	0.86 ± 0.08	B15b	22.30	17.23
42	245.04208	29.49007	0.8700	2.34 ± 0.41	0.68 ± 0.04	H08	10.41	7.56
43	345.70044	8.73083	0.7220	2.71 ± 0.40	0.75 ± 0.04	P11	23.95	19.15
44	349.63193	0.57303	0.7800	12.94 ± 2.00	1.24 ± 0.07	H08	13.13	13.51
45	349.97263	0.63699	0.8972	4.01 ± 0.38	0.80 ± 0.03	H08	15.00	13.68

Note. Column (1): cluster number sequence; Column (2)–(4): Right ascension, Declination (J2000) and redshift of a cluster; Column (5): cluster mass, M_{500} in units of $10^{14} M_{\odot}$; Column (6): cluster radius, r_{500} in Mpc; Column (7): References for cluster mass: L08 for [Lamer et al. \(2008\)](#), H08 for [Hicks et al. \(2008\)](#), V09 for [Vikhlinin et al. \(2009\)](#), M10 for [Mantz et al. \(2010\)](#), P11 for [Piffaretti et al. \(2011\)](#), R11 for [Reichert et al. \(2011\)](#), H13 for [Hasselfield et al. \(2013\)](#), T14 for [Takey et al. \(2013, 2014\)](#), G14 for [Guennou et al. \(2014\)](#), P15 for [Planck Collaboration et al. \(2015\)](#), G15 for [Gonzalez et al. \(2015\)](#), B15a for [Brodwin et al. \(2015\)](#), B15b for [Buddendiek et al. \(2015\)](#), P16 for [Planck Collaboration et al. \(2016\)](#) and T16 for [Takey et al. \(2016\)](#); Column (8): $W1$ -band total luminosity within a radius of 1 Mpc in units of L^* ; Column (9): $W1$ -band total luminosity within r_{500} in units of L^* .